




Dominating the structural, microstructural, and magnetic features of Li⁺-substituted strontium hexaferrite (Sr_{1-x}Li_{2x}Fe₁₂O₁₉)

M. M. Hessien^{1,*} , Nader El-Bagoury², M. H. H. Mahmoud¹, M. Alsawat¹, Abdullah K. Alanazi¹, and M. M. Rashad²

¹Department of Chemistry, College of Science, Taif University, P.O. Box 888, Taif 21974, Kingdom of Saudi Arabia

²Central Metallurgical Research and Development Institute (CMRDI), P.O. Box: 87, Helwan 11421, Egypt

Received: 4 March 2021

Accepted: 16 May 2021

Published online:
3 June 2021

© The Author(s), under exclusive licence to Springer Science+Business Media, LLC, part of Springer Nature 2021

ABSTRACT

Lithium ion-substituted hexagonal strontium ferrite (Sr_{1-x}Li_{2x}Fe₁₂O₁₉, where $x = 0.1, 0.2,$ and 0.3) powders have been successfully fabricated using tartrate precursor route. The impact of Li⁺ content, as well as annealing temperature on the phase evolution, microstructure, and magnetic performance, was monitored by X-ray diffraction profile, scanning electron microscopy, and vibrating sample magnetometer. Single-phase hexagonal ferrite was attained at a Li⁺ ratio of 0.2 under a range of annealing temperatures, from 1000 to 1200 °C, for 2 h. An α -Fe₂O₃ impurity phase was observed at high Li⁺ ratios of 0.4 and 0.6 for all studied temperatures. The crystallo-aspect characteristics were altered with Li⁺ content and annealing temperature. The microstructure of pure hexagonal ferrite sample visualized platelet-like structure. A fine spherical with platelet shapes were displayed by increasing the Li⁺ ratios up to 0.4 and 0.6. Energy dispersive X-ray analysis emphasized that the Fe, Sr, O, and Li atoms spread between the plate and spherical shapes. A good saturation magnetization ($M_s = 60.88$ emu/g) was realized at 0.2 Li⁺ ratio as the result of increasing the thickness of the nanoplatelet structure.

1 Introduction

Magnetic materials are important electronic materials that have a wide range of industrial and commercial applications. Magnetic materials can be regarded as being indispensable in modern technology. They are components of many electromechanical and electronic devices. Magnetic materials are also used as

components in a wide range of industrial and medical equipment. Permanent magnet materials are essential in devices for storing energy in a static magnetic field. Major applications involve the conversion of mechanical to electrical energy and vice versa, or the exertion of a force on soft ferromagnetic objects. The applications of magnetic materials in information technology are continuously growing.

Address correspondence to E-mail: m.hessien@tu.edu.sa

There are five categories of permanent magnets: Samarium cobalt (SmCo) alloys [1–3], Steels alloys (Fe alloys containing Co, Cr and W) [3], neodymium iron boron alloys (NdFeB) [4], Alnico alloys (AlNiCo) [5], and hexaferrites [3]. Due to the lower raw material cost and compositional variability than other types of materials, hexaferrites were widely used in making permanent magnets.

Growing demand for hexaferrites (M, W, X, U, Y, Z types) for daily life uses has been recorded throughout the last decades. Among them, M-type strontium-based hexaferrite ($\text{SrFe}_{12}\text{O}_{19}$) has an expanded request for different industrial, military, and home equipment applications [6, 7]. In this context, $\text{SrFe}_{12}\text{O}_{19}$ emerges exceptional features involving relatively large saturation magnetization, high coercive force, outstanding Curie temperature, pronounced magneto-crystalline anisotropy, excellent chemical and thermal stability, high dielectric constant, low conductive losses, corrosion resistance, non-toxicity, and simple accessibility [8–11].

The improvement of magnetic properties of $\text{SrFe}_{12}\text{O}_{19}$ can be monitored by controlling the distribution of strontium and iron sites as well as the synthesis strategies. Several soft synthetic routes were employed to synthesize homogeneous nanomaterials [12–15]. The tartrate precursor technique was an appropriate synthesis method to attain single-phase nanocrystalline ferrite powder with narrow size distribution, uniform shape, and homogenous microstructure at relatively low calcination temperature [16].

Due to its superior properties, $\text{SrFe}_{12}\text{O}_{19}$ is a multidisciplinary technological component indispensable for refrigerator magnets, permanent magnets, recording media, automotive industries, microwave devices, sensors, biomedicine, photocatalyst, magneto-optics devices, magnetic fluids, sound devices, electric motors, generators, etc [9, 17–20]. Consequently, enhancing the magnetic feature of strontium hexaferrite has been a theme of comprehensive examination work. Nevertheless, the substitution of Fe^{3+} or Sr^{2+} sites is an effective route to monitor the magnetic properties of strontium hexaferrite. Many previous published works are focused on the manipulation of rare earth elements, Bi^{3+} [19], Mn^{3+} [20], Co^{3+} [21], Cr^{3+} [22], or combined of divalent or trivalent ions with rare earth elements [23–26]. However, the manipulation of Li^+ substitution (as alkaline earth metal) at Sr^{2+} sites on the structural

and magnetic properties of M-type strontium ferrite is not mentioned in the literature. Therefore, in this report, the impact of Li^+ ion substitution at the Sr^{2+} sites on the structural, microstructure, and magnetic properties was investigated in details. Li^+ -substituted strontium hexaferrite ($\text{Sr}_{1-x}\text{Li}_x\text{Fe}_{12}\text{O}_{19}$) was fabricated through tartaric acid precursor approach at different ratios of Li^+ (0.2–0.6) and varied temperatures (1000–1200 °C).

2 Experimental

2.1 Materials and procedure

Anhydrous iron (III) chloride FeCl_3 (Sigma Aldrich), lithium chloride anhydrous LiCl (Fluka), strontium chloride hexahydrate $\text{SrCl}_2 \cdot 6\text{H}_2\text{O}$ (RIEDEL-DE HAEN), and tartaric acid $\text{C}_4\text{H}_6\text{O}_6$ (RIEDEL-DE HAEN) exploited in this work were employed without any further purification. Flow sheet diagram for synthesis Li ion-substituted $\text{SrFe}_{12}\text{O}_{19}$ powders ($\text{Sr}_{1-x}\text{Li}_x\text{Fe}_{12}\text{O}_{19}$ where $x = 0.1, 0.2$ and 0.3) using tartrate precursor approach is shown in Fig. 1. The next steps were similar to the previously published works elsewhere [9]. Table 1 represents the estimated weights of starting materials applied for synthesis of hexagonal ferrite powders at different Sr:Fe:Li molar ratios.

2.2 Physical properties

Crystal structure of the synthesized powders was identified by an X-ray diffractometer, model Bruker AXS (D8-ADVANCE) with $\text{Cu K}\alpha$ ($\lambda = 1.54056 \text{ \AA}$) radiation, operating at 40 kV and 10 mA. Crystallite size, lattice parameters, aspect ratio (a/c), and unit cell volume were estimated by equations in work published by Hessian et al. [9]. Scanning electron microscopy (SEM) was employed to demonstrate the change in microstructure through surface morphology and average particle size of the synthesized ferrite. Magnetic properties of the elaborated powders were defined using a vibrating sample magnetometer (VSM, 7410-LakeShore, USA) at room temperature in a maximum applied field of 20 kOe.

Fig. 1 Flow sheet diagram for synthesis of $Sr_{1-x}Li_{2x}Fe_{12}O_{19}$ using tartrate precursor approach

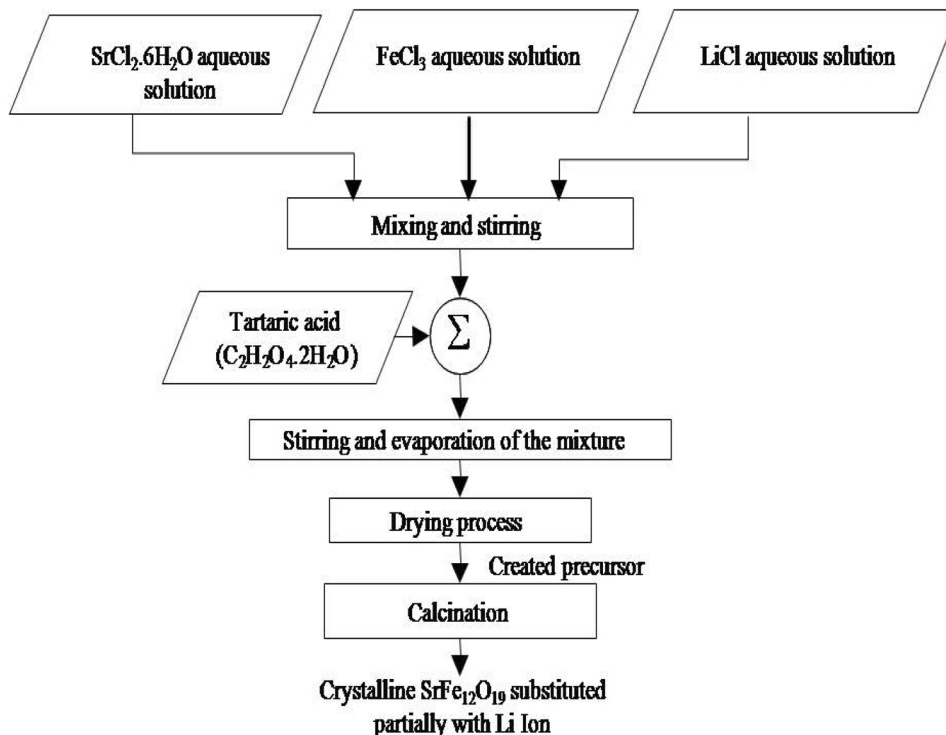


Table 1 Synthesis conditions of Li-substituted strontium hexaferrite powders

Charge No	Conditions		Target
	Charges in mol (M)	Charges in gram (g)	
1	1.0 M $SrCl_2 \cdot 6H_2O$ + 12 M $FeCl_3$ + 19 M $C_4H_6O_6$	$(\frac{266}{k})g$ $SrCl_2 \cdot 6H_2O$ + $(\frac{1946}{k})g$ $FeCl_3$ + $(\frac{2851}{k})g$ $C_4H_6O_6$	$SrFe_{12}O_{19}$
2	0.9 M $SrCl_2 \cdot 6H_2O$ + 0.2 M $LiCl$ + 12 M $FeCl_3$ + 19 M $C_4H_6O_6$	$(\frac{239.9}{k})g$ $SrCl_2 \cdot 6H_2O$ + $(\frac{8.4}{k})g$ $LiCl$ + $(\frac{1946}{k})g$ $FeCl_3$ + $(\frac{2851}{k})g$ $C_4H_6O_6$	$Sr_{0.9}Li_{0.2}Fe_{12}O_{19}$
3	0.8 M $SrCl_2 \cdot 6H_2O$ + 0.4 M $LiCl$ + 12 M $FeCl_3$ + 19 M $C_4H_6O_6$	$(\frac{21}{k})g$ $SrCl_2 \cdot 6H_2O$ + $(\frac{16.9}{k})g$ $LiCl$ + $(\frac{1946}{k})g$ $FeCl_3$ + $(\frac{2851}{k})g$ $C_4H_6O_6$	$Sr_{0.8}Li_{0.4}Fe_{12}O_{19}$
4	0.7 M $SrCl_2 \cdot 6H_2O$ + 0.6 M $LiCl$ + 12 M $FeCl_3$ + 19 M $C_4H_6O_6$	$(\frac{186}{k})g$ $SrCl_2 \cdot 6H_2O$ + $(\frac{25.4}{k})g$ $LiCl$ + $(\frac{1946}{k})g$ $FeCl_3$ + $(\frac{2851}{k})g$ $C_4H_6O_6$	$Sr_{0.7}Li_{0.6}Fe_{12}O_{19}$

k is an arbitrary scaling factor

3 Results and discussion

3.1 Phase development

Li^+ -substituted strontium hexaferrite was synthesized with the Fe:Sr:Li molar ratios of 12:0.9:0.2 and annealed at different temperatures ranging from 1000 to 1200 °C for 2 h. The XRD patterns of the produced powders indicated that all peaks were perfectly corresponding to a single well-crystallined $Sr_{1-x}Li_{2x}Fe_{12}O_{19}$ at annealing temperatures from 1100 to

1200 °C without any other impurity species (Fig. 2). The change of the Fe:Sr:Li molar ratios to be 12:0.8:0.4 indicated the presence of diffraction peaks linked to secondary impurity $\alpha-Fe_2O_3$ species as presented in Fig. 3. Eventually, Fig. 4 illustrates the XRD diffraction analysis profiles with Li^+ ratio of 0.6 at Fe:Sr ratio of 12:0.7. The evince $\alpha-Fe_2O_3$ phase is predestined together with the M-type hexagonal phase under the various studied temperatures.

Fig. 2 XRD patterns of $\text{Sr}_{0.9}\text{Li}_{0.2}\text{Fe}_{12}\text{O}_{19}$ synthesized from strontium–lithium–iron tartrate precursor treated at different temperatures (1000–1200 °C) for 2 h

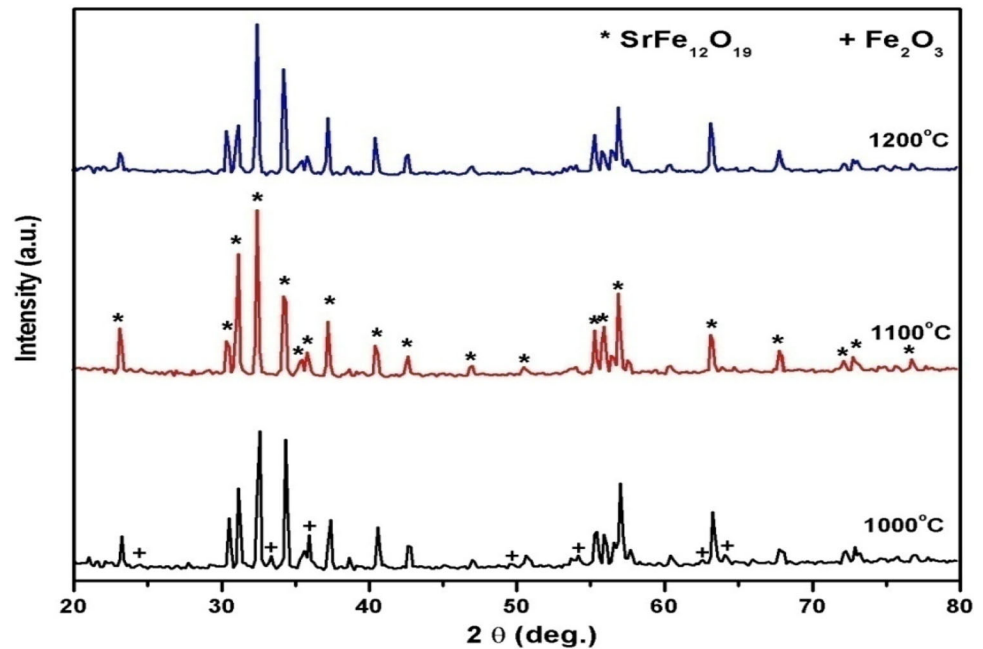
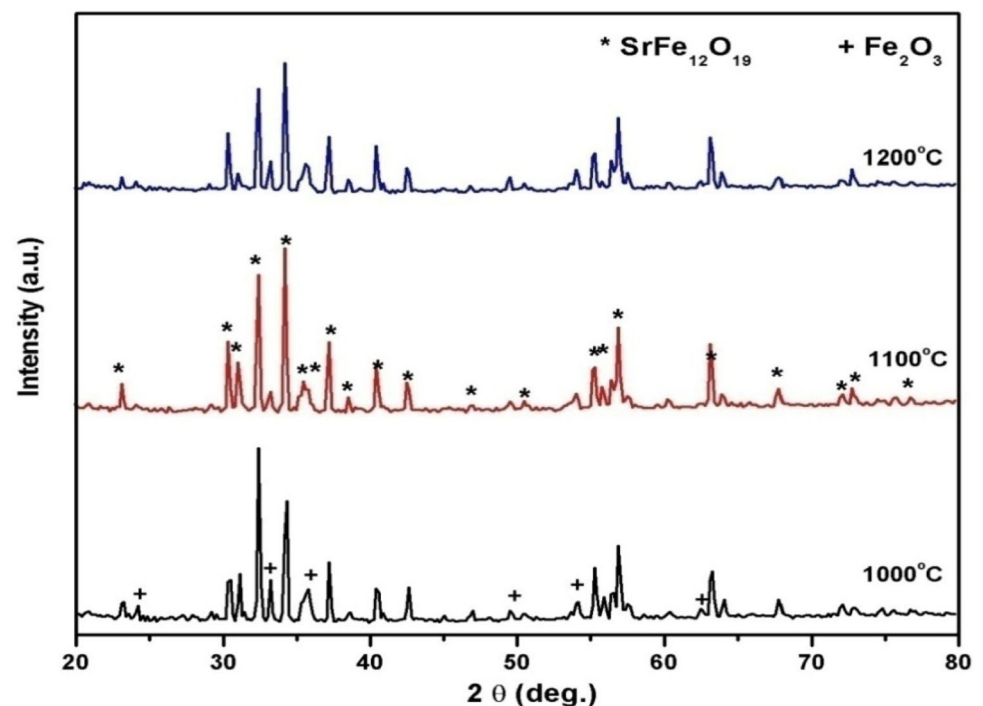


Fig. 3 XRD patterns of $\text{Sr}_{0.8}\text{Li}_{0.4}\text{Fe}_{12}\text{O}_{19}$ synthesized from strontium–lithium–iron tartrate precursor treated at different temperatures (1000–1200 °C) for 2 h



Applying Scherrer equation based on the main peak (107) of the XRD chart showed that there is variation in the crystallite size. With raising the temperature from 1000 to 1200 °C for all examined samples with Li^+ ion contents, the crystallite size of $\text{Sr}_{1-x}\text{Li}_{2x}\text{Fe}_{12}\text{O}_{19}$ was found to increase (Fig. 5; Table 2). When the annealing temperature was increased from 1000 to 1200 °C, the nanocrystalline

size of the Fe:Li molar ratio 12:0.9:0.2 was increased from 146.3 to 159.8 nm. The causes behind increasing the crystallite size with an increase of annealing temperature were the grain growing and internal stress decrease. The change of the Fe:Li molar ratio to 12:0.8:0.4 increased the nanocrystalline size. Further increasing Li^+ ion with a ratio of 0.6 on the hexagonal phase decreased the nanocrystalline

Fig. 4 XRD patterns of $\text{Sr}_{0.7}\text{Li}_{0.6}\text{Fe}_{12}\text{O}_{19}$ from strontium–lithium–iron tartarate precursor treated at different temperatures (1000–1200 °C) for 2 h

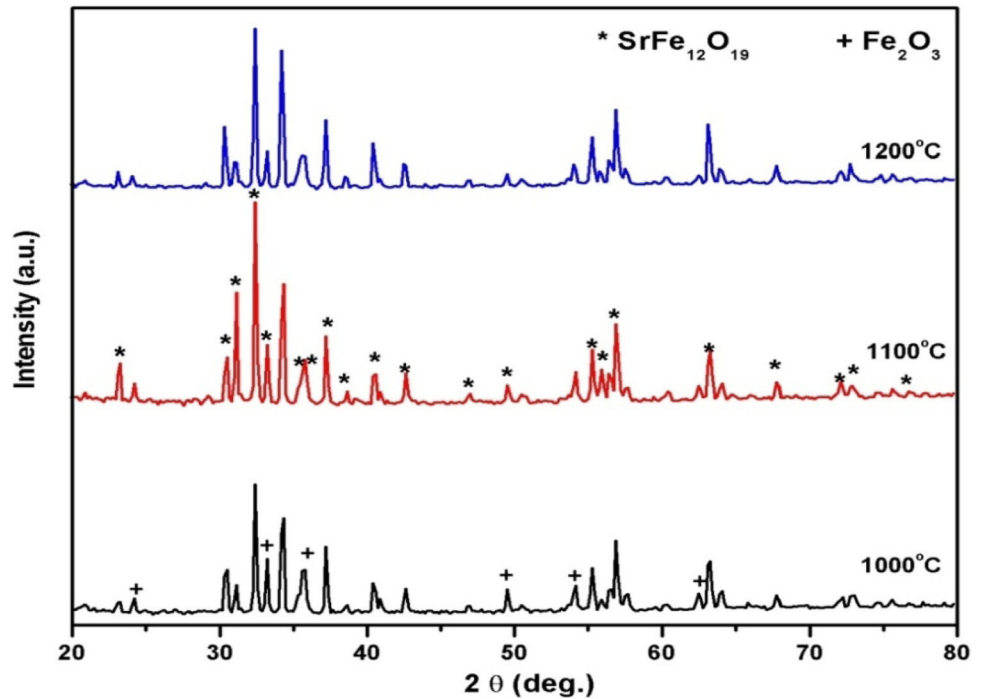
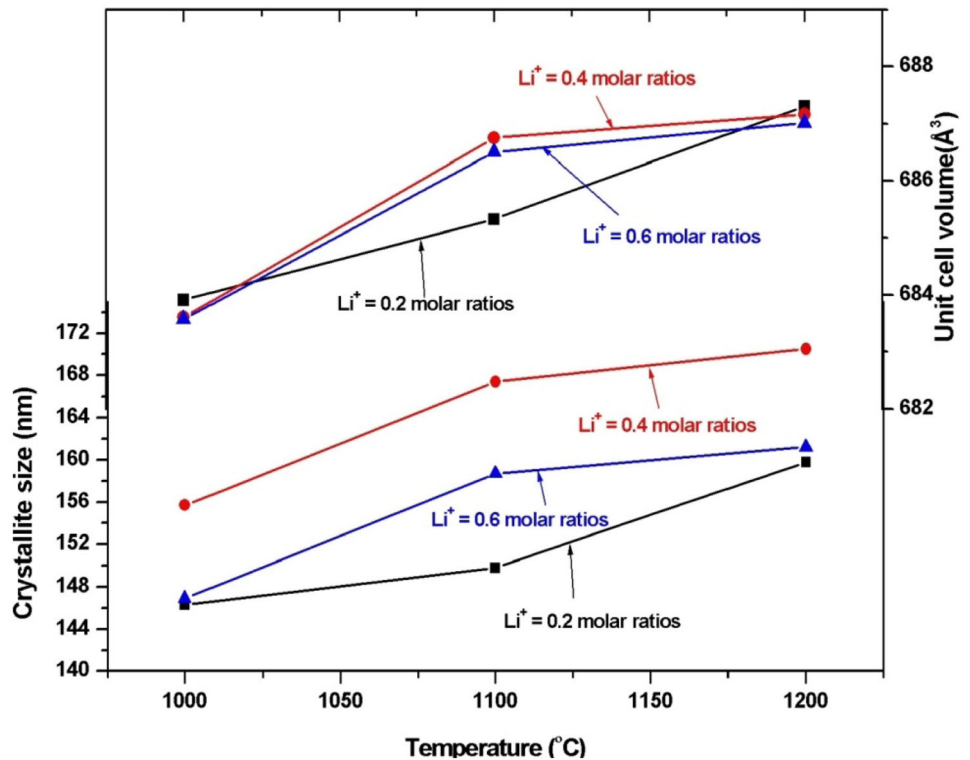


Fig. 5 Variation of crystallite size and unit cell volume as function of Li^+ ion ratio and annealing temperature



size, but still larger than that for hexagonal phase Li^+ ion with a ratio of 0.2. Noticeably, these results indicate clearly that Li^+ ion molar ratio affected on the crystallite size.

Lattice parameters are important feature that identify and reveal the structural properties of crystalline materials. Recently, determination of lattice parameters through computational approaches has gained a significant importance due to the ability to

Table 2 Crystallite size, lattice parameters, and unit cell volume on $\text{Sr}_{1-x}\text{Li}_{2x}\text{Fe}_{12}\text{O}_{19}$ nanopowder synthesized at various annealing temperatures from 1000 to 1200 °C for 2 h

Composition	Temperature, (°C)	Crystallite size, D_{xrd} , (nm)	Lattice constant			Unit cell volume, V (Å ³)
			a (Å)	c (Å)	a/c	
$\text{Sr}_{0.9}\text{Li}_{0.2}\text{Fe}_{12}\text{O}_{19}$	1000	146.3	5.6484	22.9593	3.9140	683.91
	1100	149.8	5.86218	22.96048	3.9167	685.33
	1200	159.8	5.8755	23.0223	3.918	687.30
$\text{Sr}_{0.8}\text{Li}_{0.4}\text{Fe}_{12}\text{O}_{19}$	1000	155.7	5.86388	22.95656	3.9149	683.61
	1100	167.4	5.87158	23.00168	3.9175	686.75
	1200	170.5	5.87308	23.00352	3.9168	687.16
$\text{Sr}_{0.7}\text{Li}_{0.6}\text{Fe}_{12}\text{O}_{19}$	1000	146.9	5.86298	22.9624	3.9165	683.57
	1100	158.7	5.87208	22.98944	3.9150	686.50
	1200	161.2	5.87082	22.98272	3.9147	687.01

reduce experimental temporal cost and expenses. The variation in the lattice parameters and unit cell volume of $\text{Sr}_{1-x}\text{Li}_{2x}\text{Fe}_{12}\text{O}_{19}$ with Li^+ ion ratio and annealing temperature is shown in Fig. 5 and Table 2. It can be shown that the lattice parameters and unit cell volume of $\text{Sr}_{1-x}\text{Li}_{2x}\text{Fe}_{12}\text{O}_{19}$ are influenced by the annealing temperature as well as the Li^+ ion content. The unit cell volume is effectively increased by the annealing temperatures, while Li^+ ion content had small effects on unit cell volume. The variation in the lattice parameters and unit cell volume may be related to the difference between the ionic radii of Li^+ (0.76 Å) Sr^{2+} (1.18 Å) and Fe^{3+} (0.64 Å). To determine the structure type, an examination of aspect ratio c/a can be used [8, 9, 16]. For a ratio in between 3.917 and 3.963, the M-type (magnetoplumbite) structure can be predicted. Table 2 showed that the c/a ratios of as-prepared samples (~ 3.9140 – 3.9175) are optimum M-type structure range.

3.2 Microstructure

Figure 6 displays SEM images of clear hexagonal ferrites generated through tartaric acid approaches at different Li^+ molar ratios. Hexagonal platelet-like structure was distinct with well-defined hexagonal grains and prominent grain boundaries at 0.2 Li^+ molar ratio, (Fig. 6a, b). This defined microstructure further confirms the well-crystalline $\text{SrFe}_{12}\text{O}_{19}$ phase. In contrast, further boosting Li^+ ratio to 0.4 resulted in fine spherical particles pointing the formation of secondary iron oxide composed with the hexagonal platelet shape, with wide size distributions, as

illustrated in Fig. 6c and d. Similar trends were also illustrated in Fig. 6e–h with the increase of Li^+ ratios. Meanwhile, the $\alpha\text{-Fe}_2\text{O}_3$ spherical shape was also increased.

Qualitative elemental analyses, through energy-dispersive X-ray spectroscopy (EDX), were detected on $\text{Sr}_{0.7}\text{Li}_{0.6}\text{Fe}_{12}\text{O}_{19}$ sample after heat treatment at 1100 °C to perceive allocation of each metal ion at the formation process. The EDX shown in Fig. 7 clearly indicated the characteristic charts of elemental Fe, Sr, O, and Li, and the spot analysis of $\text{Sr}_{0.8}\text{Li}_{0.4}\text{Fe}_{12}\text{O}_{19}$ - annealed at 1100 °C is presented in Table 3. It is clear that Fe, Sr, O, and Li elements were allocated between the plate-like structure (hexaferrite) and the small crystals, with larger concentration of Fe and Sr in the plate-like structure phase. Strontium was mostly presented in the plate-like structure, while lithium was mostly absent in the small crystals and in the plate-like structure. This behavior may be attributed to the loss of Li^+ content at high temperature.

3.3 Magnetic properties

Impacts of different annealing temperatures (1000, 1100, and 1200 °C) on the magnetic properties of Li^+ ion-substituted $\text{SrFe}_{12}\text{O}_{19}$ powders are illustrated in Figs. 8, 9, and 10. Values of magnetic parameters such as saturation magnetization (M_s), coercive force (H_c), remanence magnetization, and squareness ratio (M_R/M_S) are shown in Table 4. The saturation magnetization improved with increasing the annealing temperature from 1000 to 1100 °C, then diminished with further increasing the temperature up to 1200 °C. Highest saturation magnetization ($M_s =$

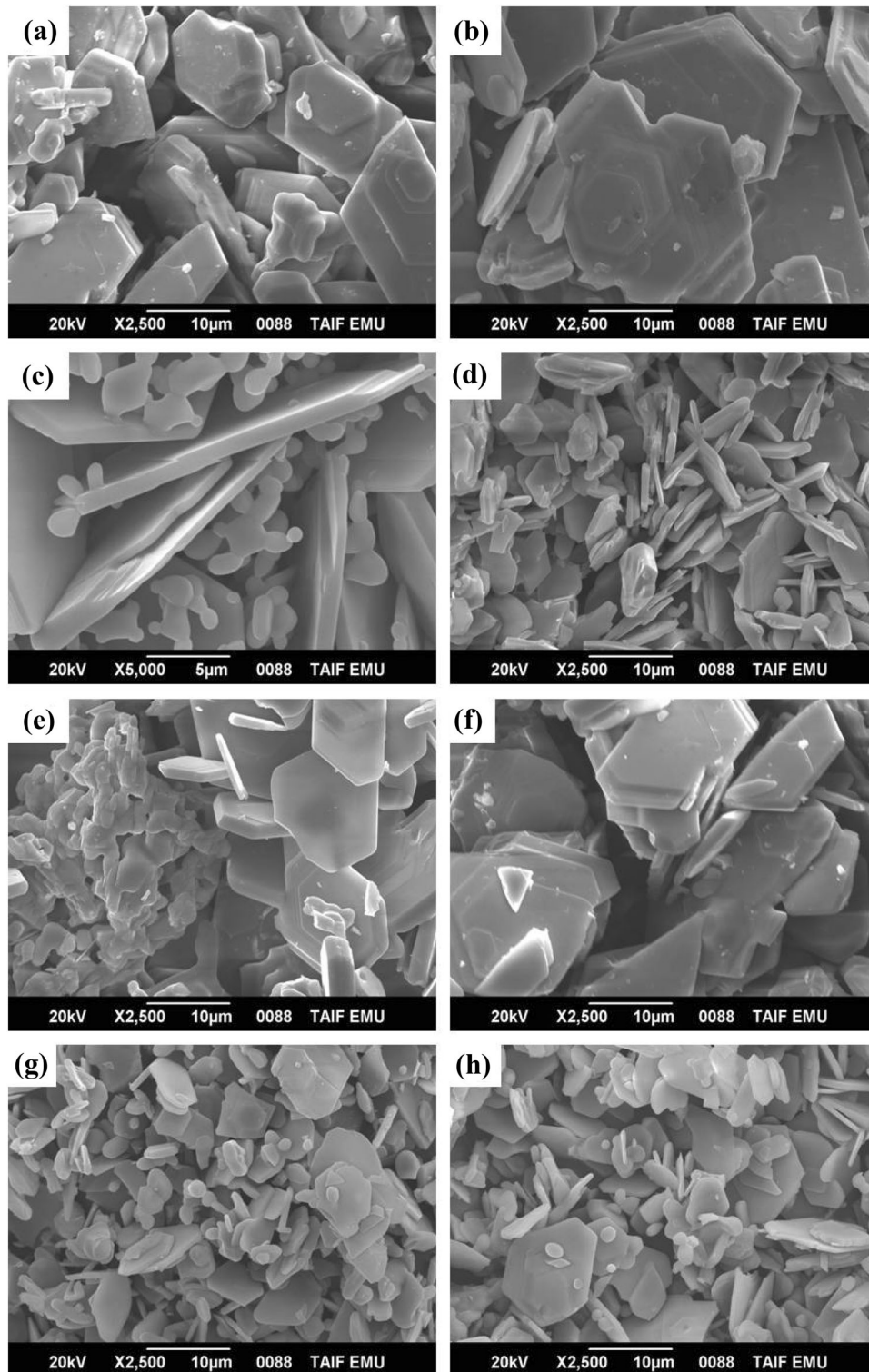


Fig. 6 SEM micrographs of $\text{Sr}_{1-x}\text{Li}_x\text{Fe}_{12}\text{O}_{19}$ nanopowders at various temperatures; **a, b** $x = 1$ and $1100\text{ }^\circ\text{C}$, **c, d** $x = 0.2$ and $1100\text{ }^\circ\text{C}$, **e, f** $x = 0.3$ and $1100\text{ }^\circ\text{C}$, and **g, h** $x = 0.3$ and $1200\text{ }^\circ\text{C}$

Fig. 7 SEM mappings of $\text{Sr}_{0.7}\text{Li}_{0.6}\text{Fe}_{12}\text{O}_{19}$ obtained at 1100 °C for the distribution of **a** real image, **b** strontium, **c** iron, **d** oxygen, **e** lithium, and **f** the associated EDX spectra

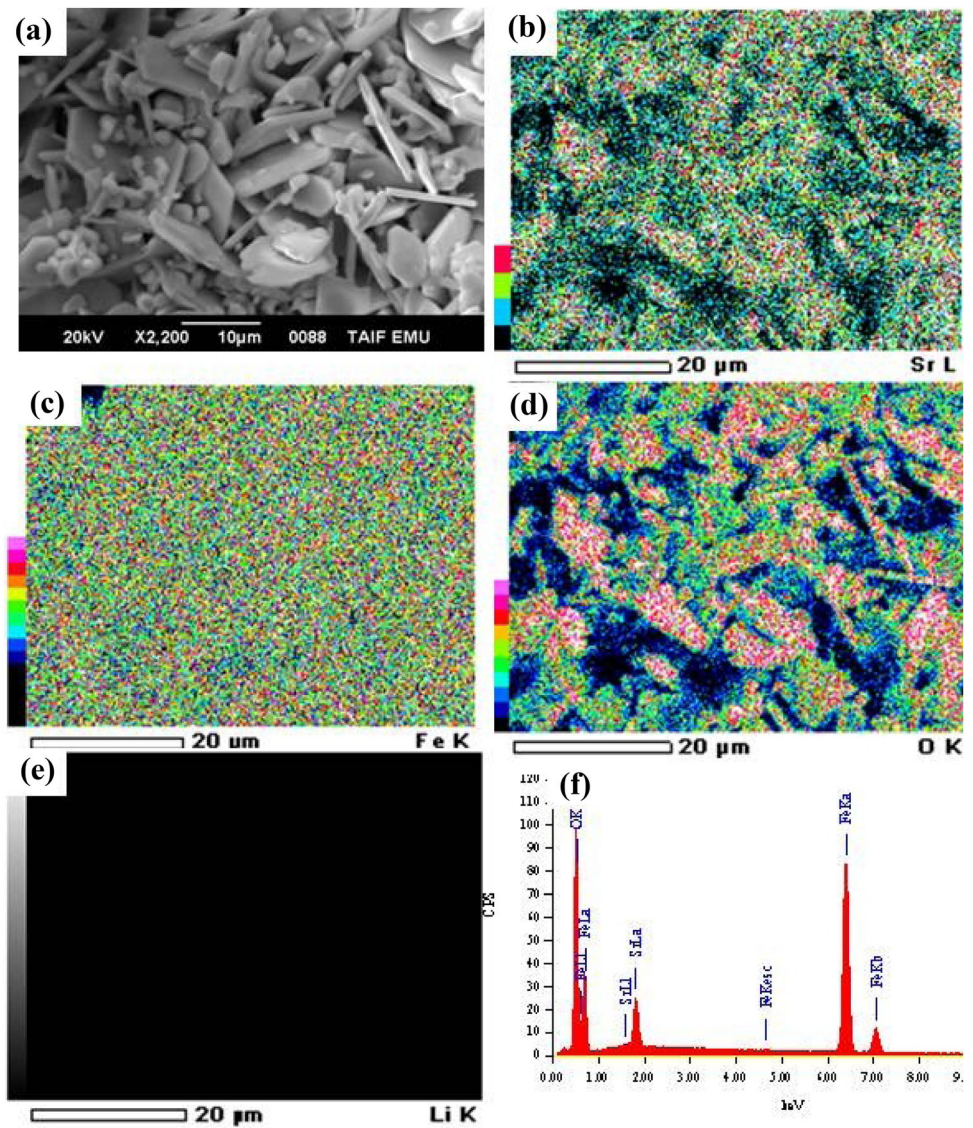


Table 3 Spot analysis range of constituent elements in the $\text{Sr}_{0.7}\text{Li}_{0.6}\text{Fe}_{12}\text{O}_{19}$ phase, wt%

Element	Sr		Fe		O		Li	
	Mass%	Atom%	Mass%	Atom%	Mass%	Atom%	Mass%	Atom%
EDX1-P1	5.69	2.94	84.07	68.10	10.25	28.97	0	0
EDX2-P1	8.13	3.04	62.36	36.57	29.51	60.40	0	0
EDX3-P2	2.47	1.29	88.51	72.80	9.02	25.91	0	0
EDX4-P2	2.29	0.79	63.67	34.61	34.05	64.60	0	0

60.88 emu/g) was acquired at 1100 °C for $\text{Sr}_{0.9}\text{Li}_{0.2}\text{Fe}_{12}\text{O}_{19}$ sample. Li et al. emphasized that the magnetic moment of hexagonal strontium ferrite platelet was improved as the thickness of nanoplatelet increased, based on magnetic force microscopy (MFM) with nanoscale spatial resolution [27] as profited in Fig. 6a, b. However, the decrease in the

saturation magnetization with increasing the Li^+ concentration at 1100 °C could correspond to the mass ratio of $\text{SrFe}_{12}\text{O}_{19}$ and $\alpha\text{-Fe}_2\text{O}_3$.

On the other hand, the coercive force of the formed Li^+ -substituted SrM ferrites was extremely reduced to lower than 1.5 KOe. Typically, H_c is rebated by both the intrinsic and extrinsic properties, such as the

Fig. 8 Effect of calcination temperature on the hysteresis loop of $\text{Sr}_{0.9}\text{Li}_{0.2}\text{Fe}_{12}\text{O}_{19}$

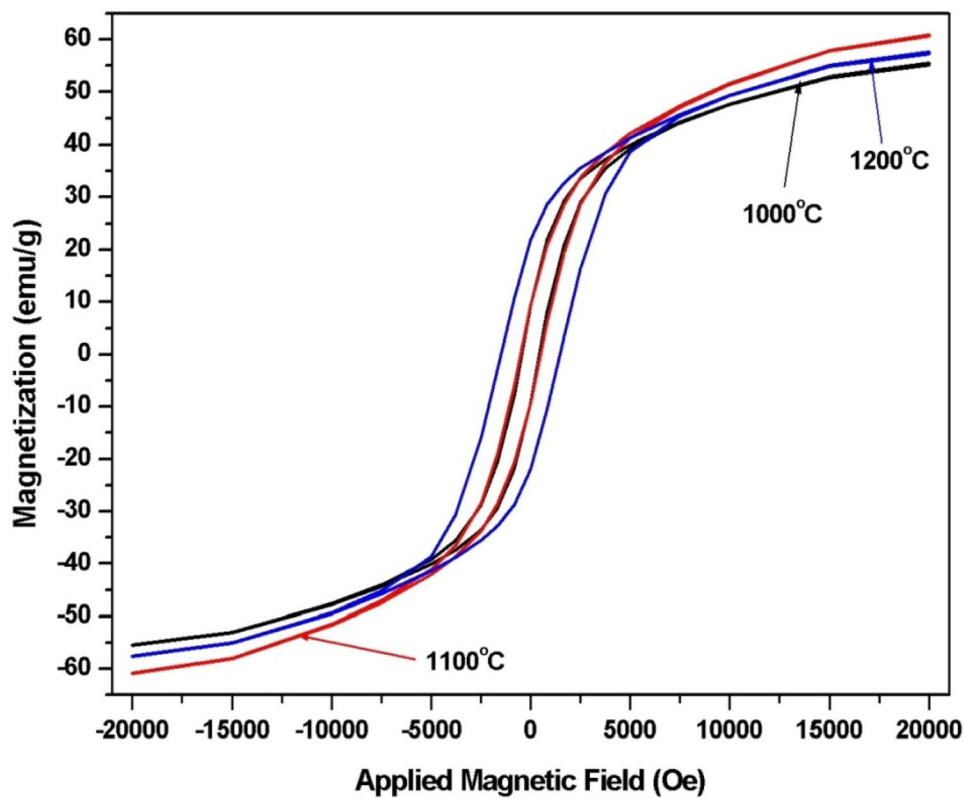


Fig. 9 Effect of calcination temperature on the hysteresis loop of $\text{Sr}_{0.8}\text{Li}_{0.4}\text{Fe}_{12}\text{O}_{19}$

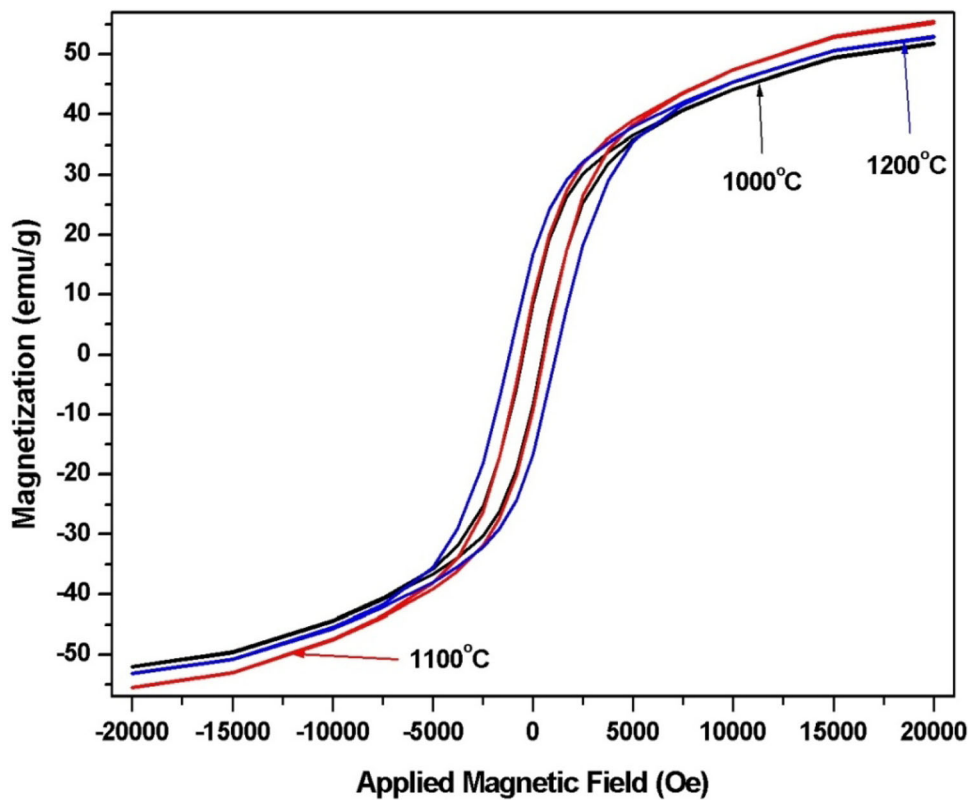


Fig. 10 Effect of calcination temperature on the hysteresis loop of $\text{Sr}_{0.7}\text{Li}_{0.6}\text{Fe}_{12}\text{O}_{19}$

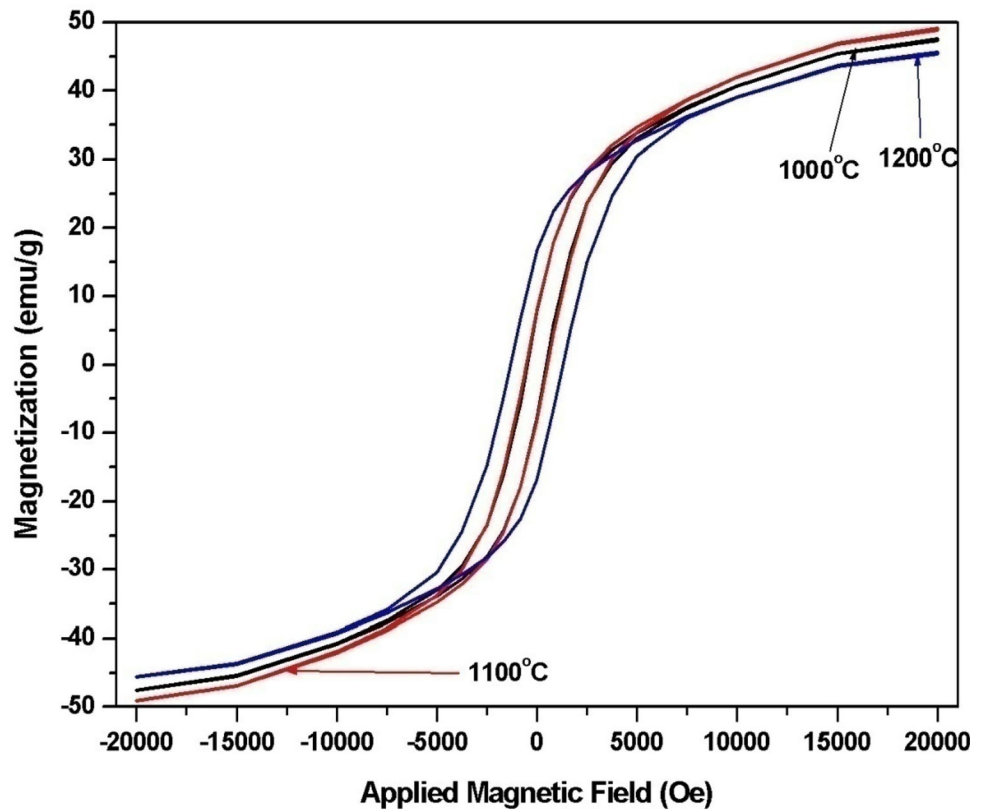


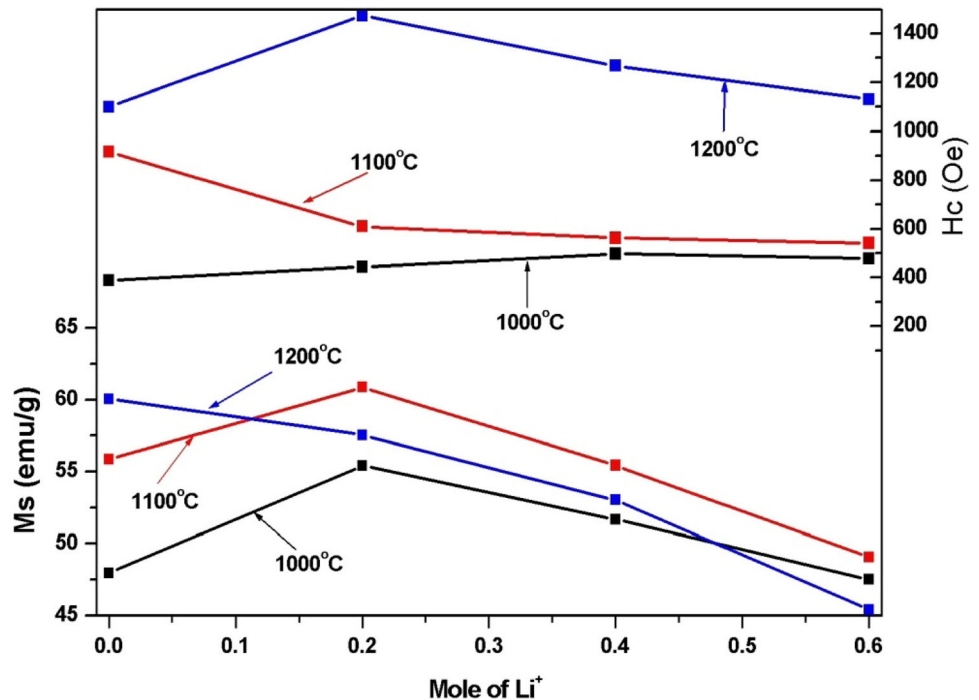
Table 4 Effect of $\text{Fe}^{3+}/\text{Sr}^{2+}$ mole ratio, La^{3+} ion substitution, and annealing temperature on the magnetic properties of the synthesized strontium hexaferrite

Composition	Temperature, (°C)	Magnetic Properties			
		Saturation magnetization M_s (emu/g)	Retentivity M_r (emu/g)	Coercivity H_c (Oe)	M_r/M_s
$\text{Sr}_{0.9}\text{Li}_{0.2}\text{Fe}_{12}\text{O}_{19}$	1000	55.41	9.18	443.9	0.166
	1100	60.88	9.34	509.74	0.153
	1200	57.55	21.99	1474.7	0.382
$\text{Sr}_{0.8}\text{Li}_{0.4}\text{Fe}_{12}\text{O}_{19}$	1000	51.69	9.18	497.58	0.178
	1100	55.44	9.51	562.83	0.172
	1200	53.02	16.78	1268.1	0.316
$\text{Sr}_{0.7}\text{Li}_{0.6}\text{Fe}_{12}\text{O}_{19}$	1000	47.53	7.74	477.29	0.163
	1100	49.05	8.144	541.25	0.166
	1200	45.60	14.59	1131.40	0.320

crystal structure, magnetic anisotropy, chemical content, composition, crystalline structure, average crystallite size, morphology, stress, lattice defects and so on [28, 29]. Based on XRD patterns and SEM specimens, it can be concluded that H_c was much dependent on the crystallinity, the average particle size, and $\alpha\text{-Fe}_2\text{O}_3$ content. In this regard, the high H_c value was related to the high average particle size

and $\alpha\text{-Fe}_2\text{O}_3$ content as well as magneto-crystalline anisotropy. The variation on the M_s and H_c values at different temperatures is shown in Fig. 11. The squareness ratios M_r/M_s of the hexagonal samples were low as the results of low crystallinity, formation of $\alpha\text{-Fe}_2\text{O}_3$ phase, and the hexagonal ferrite were in multi-magnetic domains.

Fig. 11 Variation of Saturation magnetization (M_s) and Coercivity (H_c) as function of Li^+ ion ratio and annealing temperature



4 Conclusions

A series of Li^+ ion-substituted strontium hexaferrite at different Li^+ concentrations, and annealing temperatures were tailored through on the tartaric acid precursor route. Based on structural properties, a single phase of hexagonal strontium ferrite was confirmed without impurity phase of $\text{Sr}_{0.9}\text{Li}_{0.2}\text{Fe}_{12}\text{O}_{19}$ powders at Fe:Sr:Li ratio of 12:1:0.2 and at different annealing temperatures from 1000 to 1200 °C. Increasing the Li^+ concentration in substituted SrM ferrite was found to develop the formation of $\alpha\text{-Fe}_2\text{O}_3$ as impurity phase. The lattice parameters, aspect ratio (a/c), and unit cell volumes of the formed hexaferrite powders were varied with Li^+ content and annealing temperature. The SEM investigation showed that hexagonal powders at Fe:Sr:Li molar ratio of 12:1:0.2 presented platelet-like structure at annealing temperature of 1100 °C. However, wide particle distributions of platelet and spherical shapes were distinguished with rising Li^+ molar ratio. EDX analysis revealed that Fe, Sr, O, and Li elements were spread between the platelet structure (hexaferrite) and the small spherical crystals, with a larger concentration of Fe and Sr in the plate-like structure phase. Highest saturation magnetization ($M_s = 60.88$ emu/g) was attained for $\text{Sr}_{0.9}\text{Li}_{0.2}\text{Fe}_{12}\text{O}_{19}$ sample at 1100 °C. Various coercivities (443–1474 Oe)

can be accomplished at different synthesis conditions.

References

1. Z. Ma, H. Tian, L. Cong, Q. Wu, M. Yue, S. Sun, *Angew. Chem. Int. Ed.* **58**, 14509–14512 (2019)
2. Z. Ma, M. Yue, H. Liu, Z. Yin, K. Wei, H. Guan, H. Lin, M. Shen, S. An, Q. Wu, S. Sun, *J. Am. Chem. Soc.* **142**, 8440–8446 (2020)
3. M. McCraig, *Permanent Magnets in Theory and Practice*, 2nd edn. (Pentech Press, London, 1987).
4. S. Sukmara, A. Manaf, W.A. Adib, *J. Phys. Conf. Ser.* **1751**, 012065 (2021)
5. S. Ur Rehman, C. Wei, Q. Huang, Q. Jiang, A. ul Haq, J. Wang, Z. Zhong, *J. Alloys Compd.* **857**, 157586 (2021)
6. M. Zareen, N. Yasmin, I.A. Malik, M. Zahid, M.N. Ashiq, A.L. Kiran, H. Javed, M. Safdar, M. Mirza, *J. Magn. Mater.* **497**, 165943 (2020)
7. M. Khandani, M. Yousefi, S.S.S. Afghahi, M.M. Amini, M. Bikhof Torbati, *Mater. Chem. Phys.* **235**, 121722 (2019)
8. V. Turchenko, V.G. Kostishyn, S. Trukhanov, F. Damay, F. Porcher, M. Balasoiu, N. Lupu, B. Bozza, I. Fina, A. Trukhanov, J. Walisewski, K. Recko, S. Polosan, *J. Alloys Compd.* **821**, 153412 (2020)

9. M.M. Hessien, N. El-Bagoury, M.H.H. Mahmoud, M. Alswat, A.K. Alanazi, M.M. Rashad, *J. Magn. Magn. Mater.* **498**, 166187 (2020)
10. V. Banihashemi, M.E. Ghazi, I. Izadifard, *J. Mater. Sci. Mater. Electron.* **30**, 17374–17381 (2019)
11. M.A. Almessiere, Y. Slimani, S. Güner, J. van Leusen, A. Baykal, P. Kögerler, *Mater. Sci. Mater. Electron.* **30**, 11181–11192 (2019)
12. H. Liu, X.X. Li, X. Liu, Z. Ma, Z. Yin, W. Yang, Y. Yu, *Rare Met.* **40**, 808–816 (2021)
13. C. Serletis, G. Litsardakis, E. Pavlidou, K.G. Efthimiadis, *Phys. B Condens.* **525**, 78–83 (2017)
14. F. Wang, C.B. Ponton, R. Grössinger, I.R. Harris, *J. Alloy. Compd.* **369**, 170–177 (2004)
15. S. Sugimoto, K. Haga, T. Kagotani, K. Inomata, *J. Magn. Magn. Mater.* **290–291**, 1188–1191 (2005)
16. M.M. Hessien, D.A. Rayan, M.H.H. Mahmoud, A. Alhadrami, M.M. Rashad, *J. Mater. Sci. Mater. Electron.* **29**, 9771–9779 (2018)
17. A. Almessiere, Y. Slimani, A. Baykal, *Ceram. Inter.* **44**, 9000–9008 (2018)
18. M.A.P. Buzinaro, N.S. Ferreira, F. Cunha, M.A. Macêdo, *Ceram. Inter.* **42**, 5865–5872 (2016)
19. A. Auwal, H. Erdemi, H. Sözeri, H. Güngüneş, A. Baykal, *J. Magn. Magn. Mater.* **412**, 69–82 (2016)
20. M.S. Silva, N.S. Ferreira, J.M. Soares, R.B. da Silva, M.A. Macêdo, *J. Magn. Magn. Mater.* **395**, 263–270 (2015)
21. M. Balbashov, M.E. Voronchikhina, A.A. Mukhin, VYu. Ivanov, L.D. Iskhakova, *J. Crystal Growth* **524**, 125158 (2019)
22. K. Praveena, K. Sadhana, H.-L. Liu, M. Bououdina, *J. Magn. Magn. Mater.* **426**, 604–614 (2017)
23. N. Yasmin, S. Abdulsatar, M. Hashim, M. Zahid, S.F. Gillani, A. Kalsoom, M.N. Ashiq, I.M. Safdar, *J. Magn. Magn. Mater.* **473**, 464–469 (2019)
24. Z. Iqbal, M. Muneer, S. Farooq, Z. Ahamd, M. Abdul Basit, M.N. Ashiq, R.S. Gohar, M.N. Hag, M.F. Ehsan, *J. Mater. Sci. Mater. Electron.* **30**, 4658–4664 (2019)
25. T. Huang, L. Peng, L. Li, R. Wang, Y. Hu, X. Tu, *J. Rare Metals* **34**, 148–151 (2016)
26. G.A. Ashraf, R.T. Rasool, M. Hassan, L. Zhang, *J. Alloys Compd.* **821**, 153410 (2020)
27. Q. Li, J. Song, M.S. Múzquiz, F. Besenbacher, M. Christensen, M. Dong, *Sci. Rep.* **6**, 25985 (2016)
28. R. Sun, X. Li, A. Xia, S. Su, C. Jin, *Ceram. Int.* **44**, 13551–13555 (2018)
29. M.M. Hessien, M.M. Rashad, K. El-Barawy, *J. Magn. Magn. Mater.* **320**, 336–343 (2008)

Publisher's Note Springer Nature remains neutral with regard to jurisdictional claims in published maps and institutional affiliations.